Available online at www.sciencedirect.com

ScienceDirect

Journal of Magnesium and Alloys xxx (xxxx) xxx

www.elsevier.com/locate/jma

Full Length Article

# Underlying slip/twinning activities of Mg-xGd alloys investigated by modified lattice rotation analysis

Biaobiao Yang[a], Chenying Shi[a], Xianjue Ye[a], Jianwei Teng[a], Ruilin Lai[a,*], Yujie Cui[b,*], Dikai Guan[c], Hongwei Cui[d], Yunping Li[a,*], Akihiko Chiba[b]

[a] State Key Lab for Powder Metallurgy, Central South University, Changsha 410083, China
[b] Institute for Materials Research, Tohoku University, Sendai 980-8577, Japan
[c] Department of Materials Science and Engineering, University of Sheffield, Mappin Street, Sheffield S1 3JD, United Kingdom
[d] School of Materials Science and Engineering, Shandong University of Technology, Zibo 255000, China

Received 30 January 2021; received in revised form 21 April 2021; accepted 1 June 2021
Available online xxx

**Abstract**

The inconsistencies regarding the fundamental correlation between Gd content and slip (twinning) activities of Mg alloys appeal further investigations. However, the traditional slip dislocations analysis by TEM is time-consuming, and that by SEM/EBSD cannot recognize the partial slip modes. These urge a more efficient and comprehensive approach to easily distinguish all potential slip modes occurred concurrently in alloy matrix. Here we report a modified lattice rotation analysis that can distinguish all slip systems and provide statistical results for slip activities in Mg alloy matrix. Using this method, the high ductility of Mg-Gd alloy ascribed to the enhanced non-basal slips, cross-slip, and postponed twinning activities by Gd addition is quantitatively clarified.


*Keywords:* Mg-Gd alloy; Non-basal slips; Postponed twinning; Grain boundary segregation; Modified lattice rotation analysis.

## 1. Introduction

Magnesium alloys have been extensively studied for several decades ascribed to their high specific strength and significant potentials for improving energy efficiency of transportation vehicles [1–3]. However, their applications are greatly restricted due to the low formability or limited ductility. This is essentially attributed to the extremely higher (by a factor of approx. 100) Critical Resolved Shear Stress (CRSS) for non-basal slips compared to the basal slip in Mg alloys [4–8].

Alloying by rare earth elements such as Gd is one of the promising approaches to increase the non-basal slips' activities and therefore ameliorate the ductility of alloy at ambient temperature [9–16]. Stanford et al. reported a fivefold increase in ductility of extruded Mg-4.65Gd (wt.%) compared to that of extruded pure Mg [17]. Enhanced ductility by alloying Gd in other Mg alloys was also reported [18–25]. Unfortunately, no result regarding the basal and/or non-basal slips' activities of Mg-Gd alloy has been quantitatively reported to date. For the previous research of Mg-Gd alloy by calculation, the fundamental correlation between Gd and slip (twinning) activities has yet never come to a consensus. For example, CRSS of {1–100} ⟨11–20⟩ prismatic slip was reported to be strengthened by alloying Gd to Mg alloy based on VISCO-Plastic Self-Consistent (VPSC) analysis [17]. However, on the contrary, using density-functional theory (DFT), the magnitude of Generalized Planar Fault Energy (GPFE) for the prismatic slip system was calculated to be decreased by Gd alloying [26]. It is generally accepted that the softening [26], rather than the strengthening of prismatic slip by alloying with other elements [17], leads to higher ductility of Mg alloys [27–29]. Furthermore, by a Modified Analytical Embedded Atom

* Corresponding authors.
*E-mail addresses:* 133701033@csu.edu.cn (R. Lai), cuiyujie@imr.tohoku.ac.jp (Y. Cui), lyping@csu.edu.cn (Y. Li).

https://doi.org/10.1016/j.jma.2021.06.008

Method (MAEAM), the addition of Gd was calculated to increase the c/a ratio and presumably restrain the occurrence of non-basal slips [30], which is obviously contradictory with the experimentally reported enhanced activities of non-basal slips [31]. These inconsistencies reflect further experimental analysis regarding the role of Gd on the deformation behavior of Mg is necessary.

To date, the investigations on slipping behaviors of Mg alloys mostly relied on Scanning Electron Microscopy (SEM) and/or Electron Backscattered Diffraction (EBSD) based slip traces and Transmission Electron Microscopy (TEM) based slip dislocations analysis [10], [32–37]. Unfortunately, slip traces analysis requires complicated and expensive in-situ apparatus, considering the high-quality requirement for surface. Moreover, only vast dislocation slip activities are recognized to form discernable slip traces, indicating partial dislocations were neglected during the analysis. Using TEM, although it is possible to distinguish all types of slip dislocations, to obtain slip dislocation statistics using such method is difficult and time-consuming since only limited grains can be observed for each TEM sample. In the last decade, EBSD based in-grain mis-orientation axes (IGMA) analysis proposed by Chun et al. [38] was utilized to analyze the slip behaviors [32],[38–40]. This approach is based on slip-induced lattice rotation, whose theory can be traced back to 1960s [41]. Given it's more convenient to determine dominant slip mode in alloy matrix compared to slip traces/dislocations analysis, IGMA analysis has attracted many researchers' attentions [42–46]. However, these studies by IGMA were still limited into single dominant slip mode without other slip modes being discussed to date [42–44]. And further investigations involved with various deformation modes, which can better reflect the intrinsic deformation mechanism of alloy, was not reported to the best of our knowledge.

In this work, based on previous studies using IGMA and lattice rotation analysis [32,38–40,42–44,47], a novel EBSD based modified lattice rotation analysis is proposed to theoretically predict all the potential slip systems, offering the potentials to distinguish all the activated slip types and statistically present the relative activities of all slip types. Using this novel method, the underlying deformation behaviors of Mg-xGd ($x$ = 0, 0.3, 1) (at.%) alloys under various strains were investigated thoroughly. Twinning behaviors were also analyzed using MTEX in-house codes [48]. This work will provide valuable insights toward development of novel high-performance Mg alloys.

## 2. Materials and methods

Three Mg-xGd ($x$ = 0, 0.3, 1) (at.%) alloy ingots were prepared by vacuum melting using commercial-purity Mg (99.95 wt.%) and Mg-30Gd (wt.%) master alloy, following by homogenization treatment at 400 °C for 2 h and air cooling. The alloy was hot extruded at 300 °C with an extrusion ratio of 16:1 and a ram speed of approx. 2 mm•$s^{-1}$, respectively, subsequently following by heat treatment again at 400 °C for 2 h and air cooling. The obtained alloys were cut into cylinders with a height and a diameter of 15 and 10 mm, respectively. The compression direction was parallel to Extruded Direction (ED). The compression tests were performed using MTS landmark materials testing system (MTS Systems Corporation, Eden Prairie, MN, USA) with a displacement speed of 0.05 mm•$min^{-1}$ at room temperature.

Table 1
Slip systems for the Mg alloy and corresponding Taylor axes.

| Slip types | Slip systems | Number of slip variants | Taylor axis | Number of Taylor axis variants |
|---|---|---|---|---|
| Basal <a> | {0001} <11−20> | 3 | <1 − 100> | 3 |
| Prismatic <a> | {1–100} <11−20> | 3 | <0001> | 1 |
| Pyramidal I ⟨a⟩ | {−1011} <−12–10> | 6 | <10−12> | 6 |
| Pyramidal I ⟨c + a⟩ | {10–11} <2 − 1–13> | 12 | <1 − 32–1> | 12 |

The microstructures and textures of Mg-xGd alloys before and after compression tests were captured using field emission scanning electron microscopy (FESEM, FEI XL30S, FEI Company, Portland, OR, USA; spot size: 3.5, accelerating voltage: 20 kV) equipped with electron backscattered diffraction (EBSD, Oxford HKL Channel 5, Oxford Instruments, Abingdon, UK) and energy dispersive spectrometer (EDS, Oxford Instruments, Abingdon, UK). Specimens for FESEM and EBSD were mechanically polished using SiC paper, 0.5, 0.05 $\mu$m diamond slurries, and finally 40 nm oxide polishing suspensions (OPS) solution for 15 min. Postmortem analysis on twinning and slip behaviors were performed using HKL Channel 5.0 and MATLAB with in-house MTEX codes [48]. Transmission electron microscopy (TEM, Talos F200X, FEI Company, Portland, OR, USA) was also utilized to analyze the microstructure near grain boundaries. Specimens for TEM were first cut to a thin disk of 500 $\mu$m, mechanically grounded down to 50 $\mu$m, then perforated by a twin-jet electron polisher in 10% $HClO_4$ + 90% $C_2H_5OH$ at 23 V and −25 °C for 30 s, and finally ion milled by a 5 keV Ar-ion beam at ˜2° for 30 min.

The modified lattice rotation analysis proposed to predict projection traces in pole figures by rotating parent grain along different Taylor axes with a fixed rotation angle of 5° is illustrated in Fig. 1. The initial orientation of parent grain is obtained in the region with the smallest kernel average misorientation (KAM) value. Taylor axis ($\overrightarrow{T_S}$) is the cross product between the unit normal vector of slip plane ($\overrightarrow{n_s}$) and the slip direction vector ($\overrightarrow{d_s}$) by following equation:

$$\overrightarrow{T_S} = \overrightarrow{n_s} \times \overrightarrow{d_s} \quad (1)$$

Given that recent studies still didn't come to a consensus regarding whether ⟨c + a⟩ slip dislocation locates in pyramidal I {10–11} plane or pyramidal II {11–22} plane, only pyramidal I {10–11} ⟨c + a⟩ slip dislocation was considered for analysis [14,49]. All possible slip systems calculated in this work are summarized in Table 1. Note that this modi-

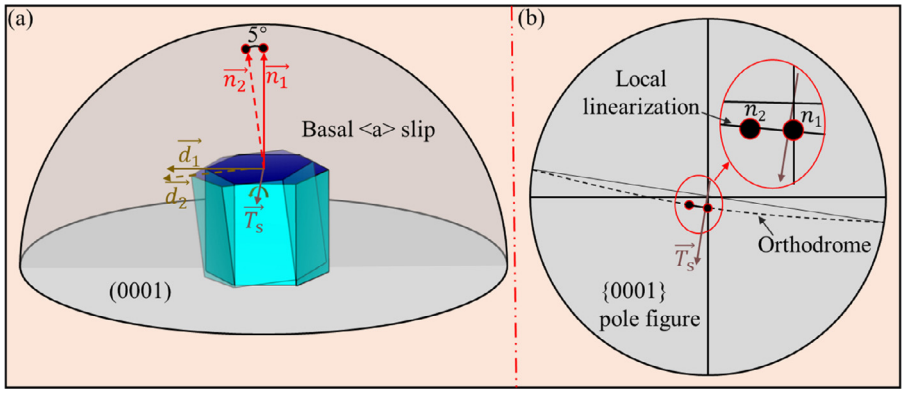


Fig. 1. (a-b) Schematic illustration for the lattice rotation mechanism during deformation, where (a) $\overrightarrow{d_1}$, $\overrightarrow{d_2}$, $\overrightarrow{n_1}$, $\overrightarrow{n_2}$, and $\overrightarrow{T_s}$ are the initial slip shear direction, the postmortem slip shear direction, the initial vector of c-axis, the postmortem vector of c-axis and the Taylor axis, respectively. (b) $n_1$ and $n_2$ are the projected points of the $\overrightarrow{n_1}$, and $\overrightarrow{n_2}$ on the {0001} pole figure, respectively.

fied lattice rotation analysis still cannot distinguish the slip systems sharing with similar rotation axis, and this intrinsic deficiency necessitates the introduction of other metrics to precisely identify active slip system in the future.

## 3. Results and discussions

Fig. 2 depicts the initial microstructures of extruded Mg-xGd alloys in terms of inverse pole figure (IPF). Obviously, IPF of pure Mg is mostly characterized with {11–20} and {10–10} planes, while that of Mg-0.3Gd and Mg-1Gd alloys exhibit relatively more uniform distributions of orientation. The grain size distributions of Mg-xGd alloys reveal that slight Gd addition (i.e., 0.3 at.%) reduces the grain size whist further grain refinement was not obtained by adding more Gd (i.e., 1 at.%), which is consistent with previous study by Stanford et al. [17]. Further analysis on the distribution of c axis to ED shows that the Gd addition randomizes the distribution of {0001} plane (Fig. 2 (g-i)). To further analyze the initial textures, {0001}, {11–20} and {10–10} pole figures of extruded Mg-xGd alloys were presented in Fig. 3. Pure Mg exhibits strong {0001} fiber texture, while the basal texture turns weaker in Mg-0.3Gd and Mg-1Gd alloys, in accordance with the results of Fig. 2 and previous studies [17,22,50–52]. Fig. 4 shows the microstructures of Mg-xGd alloys under backscattered electron (BSE) mode. With increasing Gd content, the area fraction of Gd-rich clusters (GRC) increases from 1.56% (Mg-0.3Gd) to 4.56% (Mg-1Gd), as statistically determined by Image Pro-Plus 6.0 software. In addition, GRC distribute paralleling to extruded direction (ED), related with extrusion process [53].

Fig. 5(a) presents the compressive stress-strain curves of three alloys. With increasing Gd content, the yield strength, fracture strength and fracture strain are observed to be simultaneously increasing. Both Mg-0.3Gd and Mg-1Gd alloys exhibit clear yield plateau, which can be seen in other Mg-RE alloys [17,25,54–56]. This yield plateau is presumably associated with elastic interaction and Cottrell atmosphere by Gd addition [55]. In addition, with the increase in Gd concentration, the sigmoidal (S-shaped) characteristic of twin-dominated deformation transfers gradually to the parabolic characteristic of slip-dominated deformation. To quantitatively describe this phenomenon, the work hardening rates are plotted as a function of true strain for Mg-xGd alloys, as shown in Fig. 5(b). Obviously, the peak working hardening rate is decreasing with increasing Gd content. Meanwhile, as the concentration of Gd increases, the variation amplitude of working hardening rate is declining gradually. In other words, the softening resistance of Mg alloys is obviously increasing with increasing Gd content, suggesting underlying deformation behavior is presumably altered by Gd addition.

Figs. 6 and 7 display the microstructures of Mg-xGd alloys after compression to 4 and 12%, respectively. Obviously, after compression to 4%, amounts of {10–12} tension twins can be observed in pure Mg; on the contrary, little deformation twins can be found in both Mg-0.3Gd and Mg-1Gd alloys. As compressive strain increases to 12%, {10–12} tension twins are witnessed to occupy higher area fractions than that under 4% strain and concomitantly some {10–12}-{10–12} secondary twin boundaries are observed in both pure Mg and Mg-0.3Gd alloy; however, deformation twins are still hardly observed in Mg-1Gd alloy. These suggest twinning behavior depends strongly not only on the loading strain but also on the Gd concentration. The mis-orientation angle distributions of Mg-xGd alloys under 0, 4, and 12% strains are presented in Fig. 8. Around 86 ± 5, an apparent peak with a concentrated rotation axis of [−12–10] corresponding to tension twin is observed in pure Mg (4 and 12% strains) and Mg-0.3Gd alloy (12% strain), consistent with the results of Figs. 6 and 7. In addition, with increasing strain, the intensity of low angle boundaries (LABs) increases gradually for all alloys, revealing the presence of potential slip activities.

After compression to fracture point, the microstructure of Mg-1Gd alloy is characterized using FESEM as shown in Fig. 9. Except amounts of GRC distributing along ED, numerous twins can be observed in Mg-1Gd alloy (applied with approx. 30% strain). The twinning area and number fractions of Mg-(0, 0.3, 1) Gd (at.%) alloys under various compres-

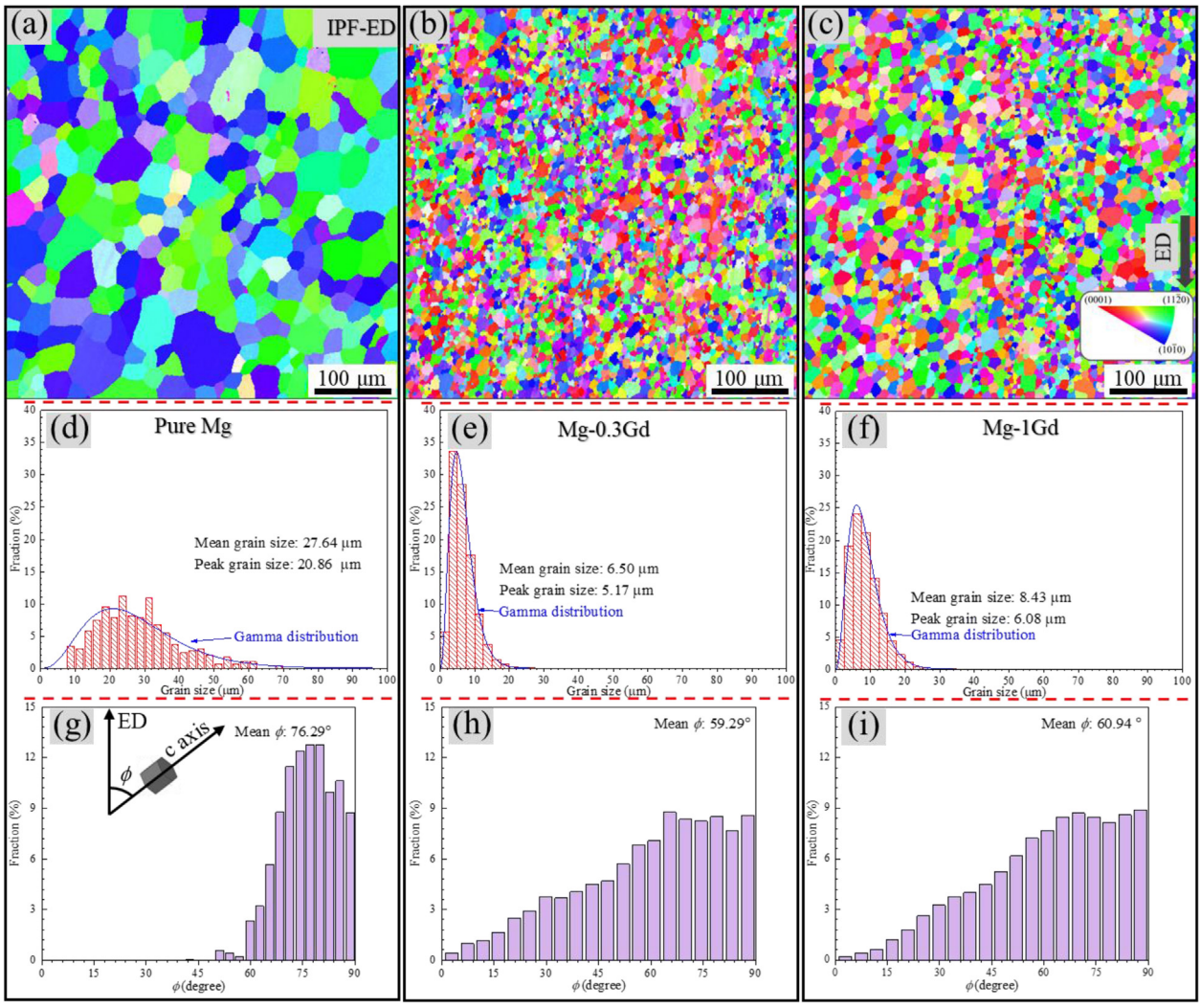


Fig. 2. The EBSD results in terms of (a-c) inverse pole figure - extruded direction (IPF-ED), (d-f) grain size statistics and (g-i) distributions of tilting angle (Φ) between ⟨0001⟩ and ED regarding (a, d, g) Pure Mg, (b, e, h) Mg-0.3Gd, (c, f, i) Mg-1Gd alloys.

Table 2
Twinning area and number fractions of Pure Mg, Mg-0.3Gd, and Mg-1Gd alloys under various strains.

| Alloys | Strain (%) | Twinning area fractions (%) | Twinning number fractions (%) |
|---|---|---|---|
| Pure Mg | 4 | 9.67 | 62.24 |
| | 12 | 75.58 | 85.51 |
| Mg-0.3Gd | 4 | 0.30 | 1.69 |
| | 12 | 5.57 | 60.38 |
| Mg-1Gd | 4 | 0.11 | 1.82 |
| | 12 | 0.28 | 1.85 |
| | 30 | – | 48.76 |

sive strains are tabulated into Table 2. Critical strain for the onset of profuse tension twins with number fraction higher than 10% seems to be increasing as Gd concentration increases from 0 to 1 at.%. In other words, Gd addition defers the presence of profuse tension twinning. Apart from that, the role of twinning behavior is also weakened by Gd addition. For example, the twinning number fraction in pure Mg after compression to 12% is approximately 85.51%, distinctly higher than that of Mg-1Gd after compression even to 30% (48.76%).

The macroscopic twinning strain ($\varepsilon_t$) can be quantitatively determined by [57],[58]:

$$\varepsilon_t = m_t \cdot \Delta f_s \cdot \gamma_t \quad (2)$$

where $m_t$ is Schmid factor for twinning, $\gamma_t$ is the tension twinning shear strain (0.126) [59], and $\Delta f_s$ represents the variation of twinning volume fraction and could be obtained based on the change of twinning area fraction ($\Delta A_T$) using the following equation [60]:

$$\Delta f_s = \Delta A_T \cdot \sin(\theta) \quad (3)$$

in which $\theta$ is the average angle between twinning plane and view plane (roughly adopted with 90° in this work). Conventionally, the Schmid factor ($m$) can be calculated by:

$$m = \cos(\varphi) \cdot \cos(\lambda) \quad (4)$$

where $\varphi$ represents the angle between twinning or slip plane normal direction and loading force, and $\lambda$ is the angle be-

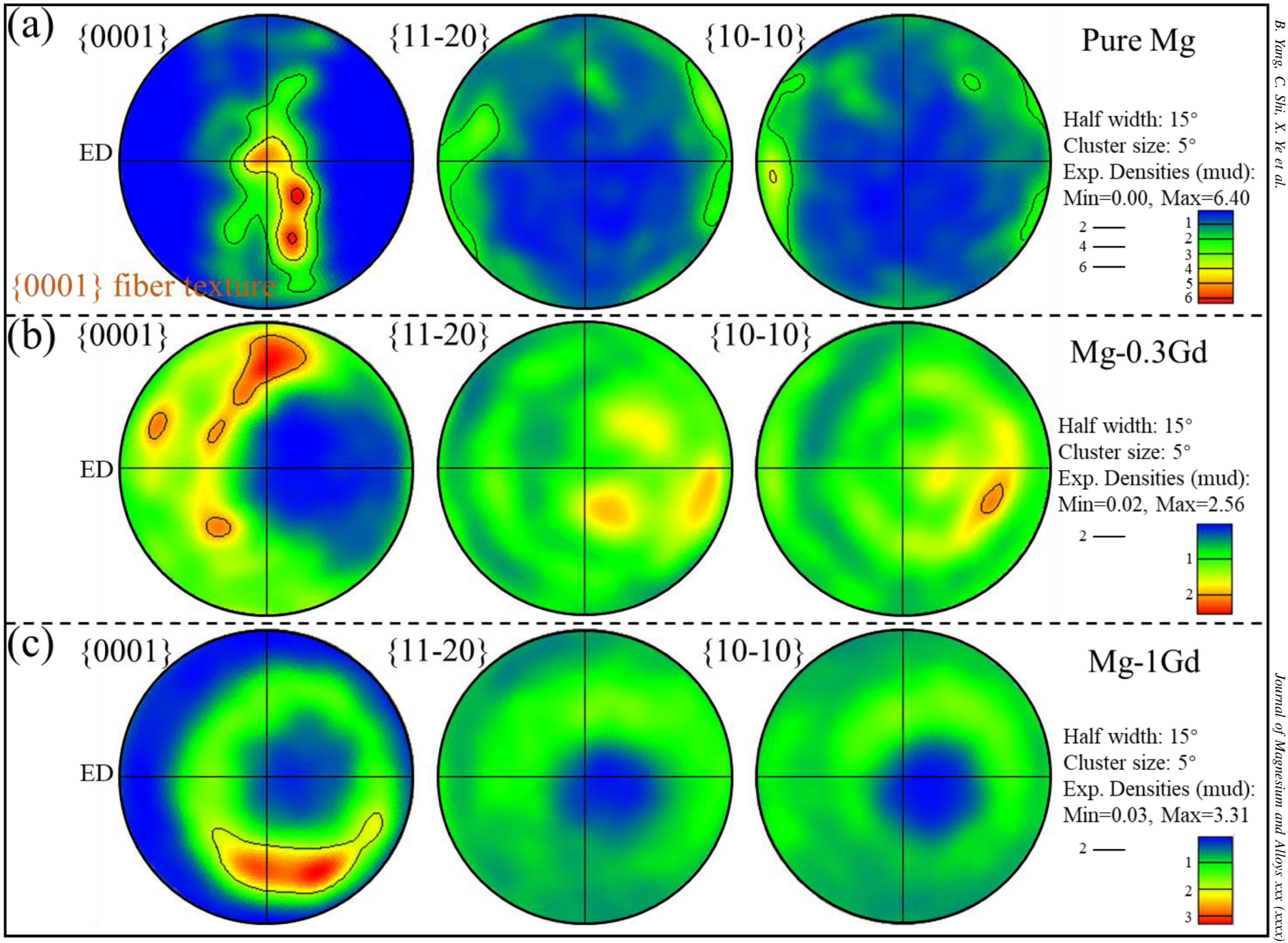


Fig. 3. {0001}, {11–20}, and {10–10} pole figures of initial (a) pure Mg, (b) Mg-0.3Gd, (c) Mg-1Gd alloys before compression tests.

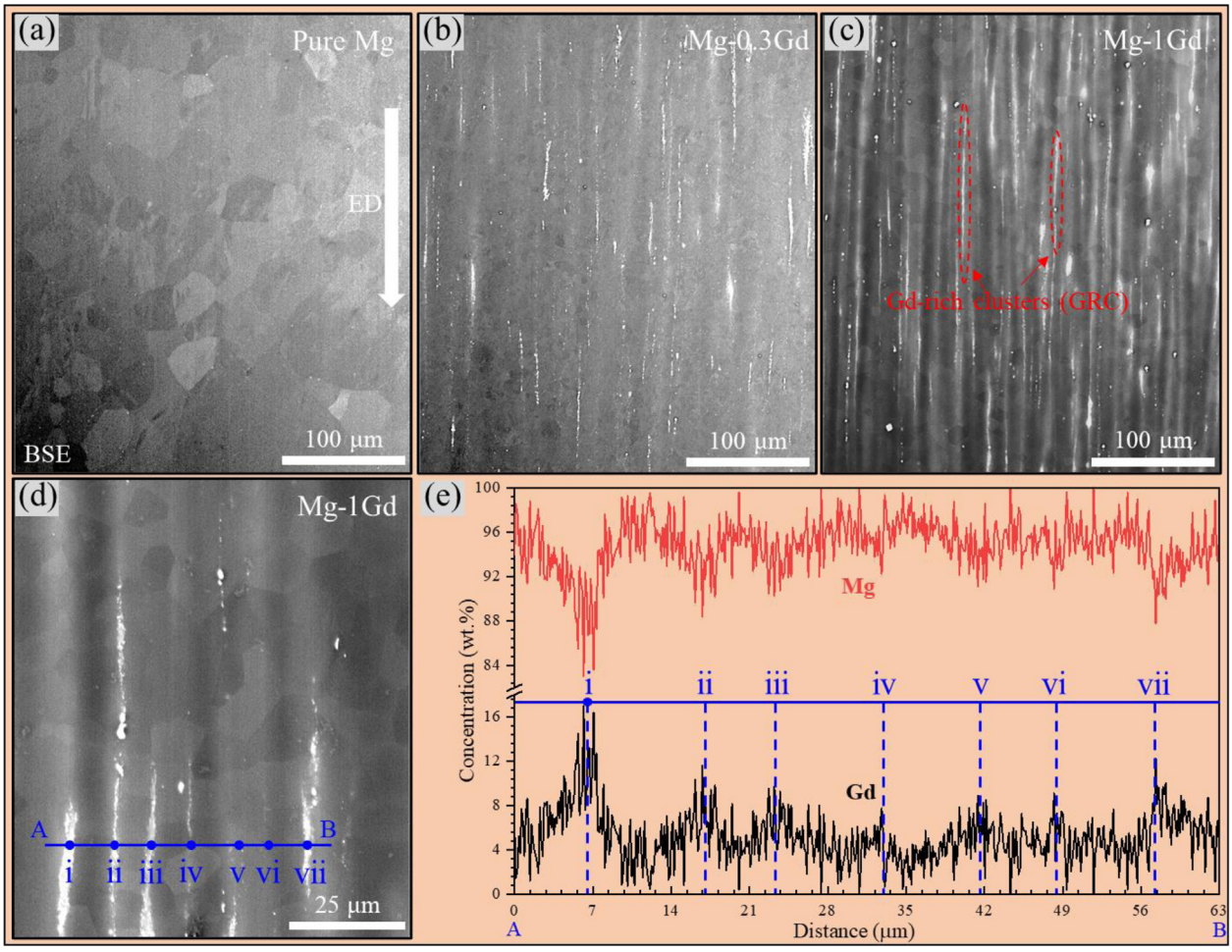


Fig. 4. (a-d) The SEM morphologies under backscattered electron (BSE) mode of (a) pure Mg, (b) Mg-0.3Gd and (c-d) Mg-1Gd alloys before compression tests. (e) EDS results of line AB shown in Fig. 4(d). (For interpretation of the references to colour in this figure legend, the reader is referred to the web version of this article.)

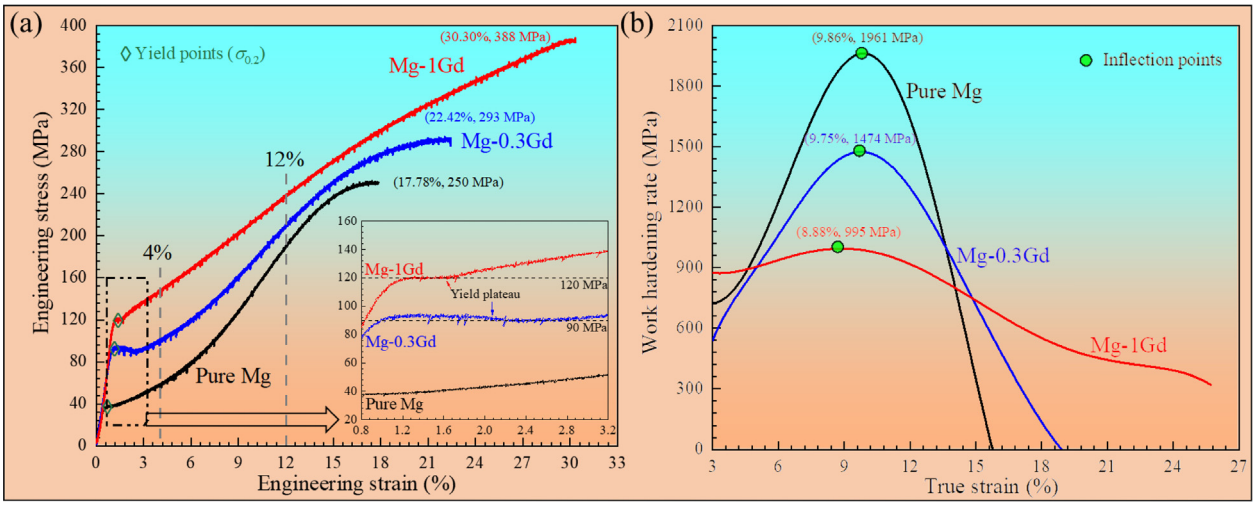


Fig. 5. (a) Compression stress-strain curves and (b) work hardening rate-true strain curves of pure Mg, Mg-0.3Gd, and Mg-1Gd alloys.

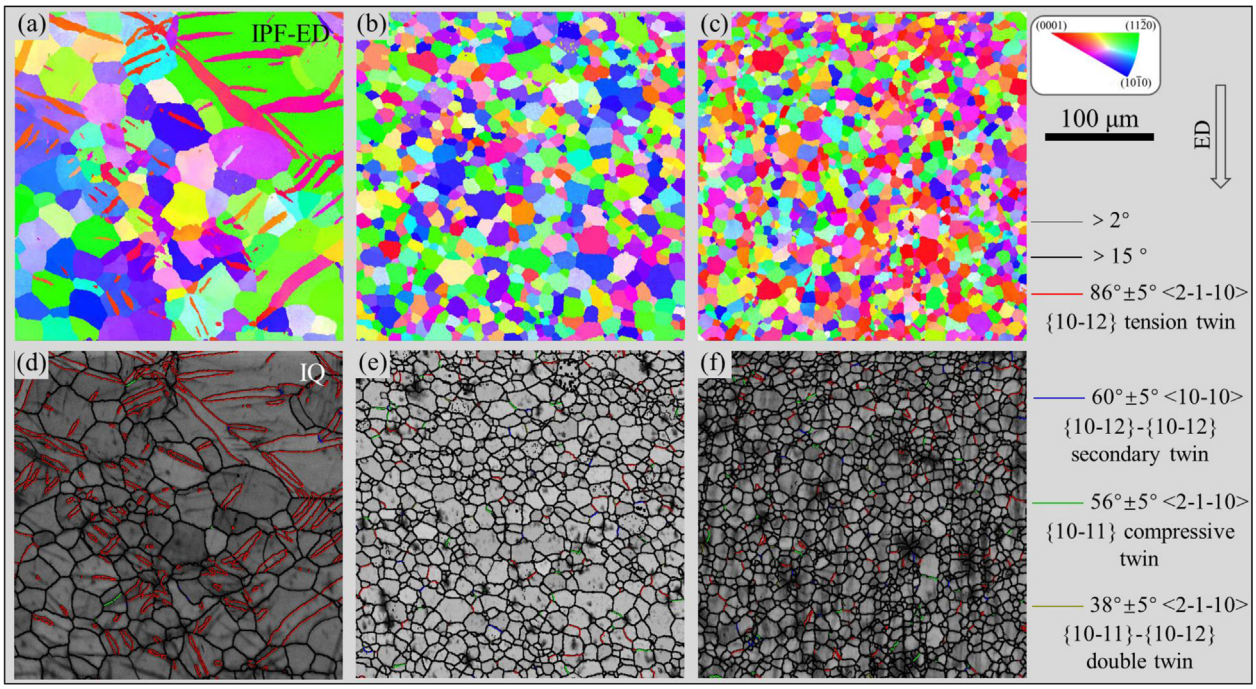


Fig. 6. EBSD results in terms of (a-c) IPF and (d-f) image quality (IQ) maps showing the microstructures of (a, d) pure Mg, (b, e) Mg-0.3Gd and (c, f) Mg-1Gd alloys after being applied 4% compressive strain.

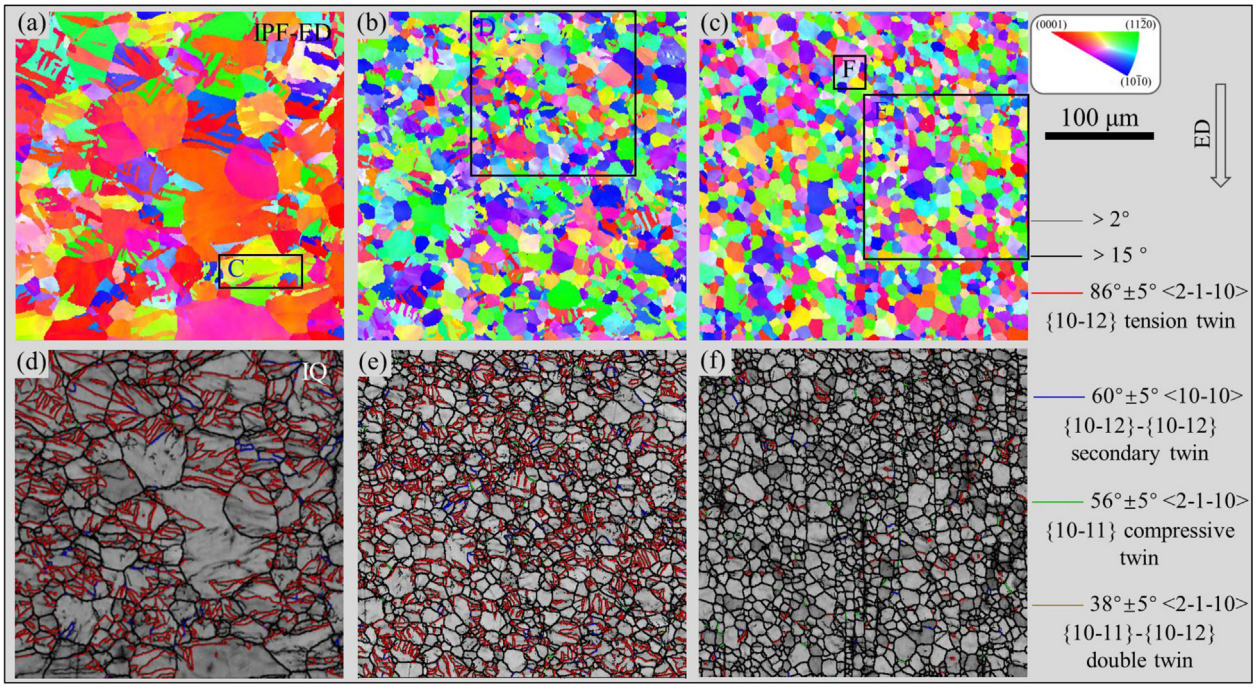


Fig. 7. EBSD results in terms of (a-c) IPF and (d-f) image quality (IQ) maps showing the microstructures of (a, d) pure Mg, (b, e) Mg-0.3Gd and (c, f) Mg-1Gd alloys after being applied 12% compressive strain.

tween twinning or slip shear direction and loading force. By assuming two specific conditions (<11−20>//ED and <1 − 100>//ED), four potential twinning modes can be predicted according to vector geometry [61] and corresponding $m_t$ variation as a function of tilting angle (Φ) between ⟨0001⟩ and ED (Fig. 10) can be expressed by the following equation:

$$m_t = \begin{cases} -\frac{1}{2}\cos^2\Phi \ (T1-1) \\ -\frac{1}{2}\cos^2\Phi + \frac{3}{8}\sin^2\Phi \ (T1-2) \\ -\frac{1}{2}\cos 2\Phi \ (T2-1) \\ -\frac{1}{2}\cos^2\Phi + \frac{1}{8}\sin^2\Phi \ (T2-2) \end{cases} (0^\circ \le \Phi \le 180^\circ) \quad (5)$$

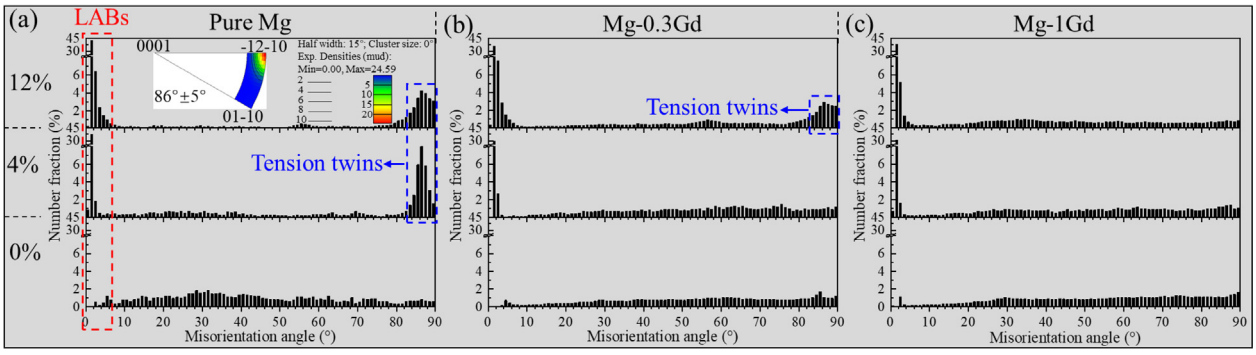


Fig. 8. Mis-orientation angle distributions of (a) pure Mg, (b) Mg-0.3Gd, (c) Mg-1Gd alloys after being applied 0, 4 and 12% compressive strains.

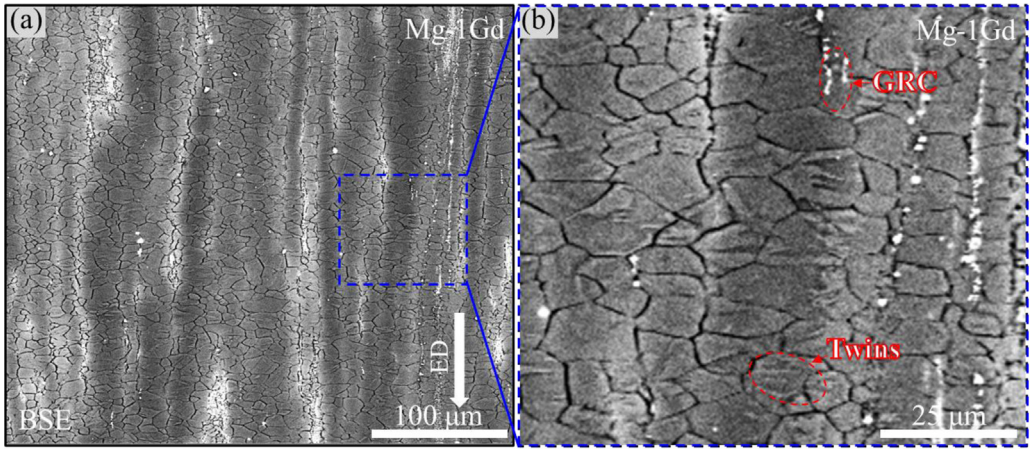


Fig. 9. (a-b) The SEM morphologies under BSE mode of Mg-1Gd alloy captured with two different magnifications after the fracture of compression. (For interpretation of the references to colour in this figure legend, the reader is referred to the web version of this article.)

Table 3
Calculated twinning strain and its contributions for various alloys after compression of 4 and 12% strains.

| Alloys | $\gamma_t$ | $m_t$ | Total strain (%) | $\Delta f_s$ (%) | Twinning strain (%) | Twinning strain contribution (%) |
|---|---|---|---|---|---|---|
| Pure Mg | 0.13 | 0.23–0.43 | 4 | 9.67 | 0.28–0.52 | 7.00–13.00 |
| | | | 12 | 75.58 | 2.19–4.09 | 18.25–34.08 |
| Mg-0.3Gd | | 0.09–0.26 | 4 | 0.30 | 0.003–0.01 | 0.08–0.25 |
| | | | 12 | 5.57 | 0.06–0.18 | 0.50–1.50 |
| Mg-1Gd | | 0.09–0.27 | 4 | 0.11 | 0.001–0.004 | 0.03–0.10 |
| | | | 12 | 0.28 | 0.003–0.01 | 0.03–0.08 |

By integrating the positive part shown in Fig. 10 with the distributions of tilting angle (Φ) of Fig. 2 (g-h), the upper (T2–1) and lower (T1–2) bounds of $m_t$ are roughly determined (Table 3). Corresponding twinning strains can be further calculated based on Eq. (2) (Table 3). Evidently, under similar 12% compressive strain, twinning takes a considerable proportion (approx. 18.25–34.08%) of the deformation for pure Mg, whilst twinning contribution was lower than 1.5% strain in other Gd-containing alloys, suggesting the Gd addition significantly suppresses twinning activities. This reveals non-basal slips should presumably have been activated and taken large proportions in deformation of Mg-Gd alloys to meet the von Mises criterion [5].

To ascertain the presence of non-basal slip modes, a representative example of modified lattice rotation analysis was presented in Fig. 11. The conventional IGMA distribution of Region of Interest (ROI) C with the concentration of rotation axis nearing [01–10] axis implies numerous basal slip activities were activated (Fig. 11(b)). According to modified lattice rotation analysis, by comparing the experimental projection results and theoretical predictions of ideal slip-induced orientation gradients for ROI C, basal ⟨a⟩, prismatic ⟨a⟩, pyramidal I ⟨a⟩ and pyramidal I ⟨$c$ + $a$⟩ slips are distinguished clearly for both parent grain 1 (Fig. 11 (c-d) P1-P5) and twin 1 (Fig. 11 (c-d) T1-T5). The obvious transformations of slip rotation axes in Fig. 11 reveal the potential cross-slip behavior. Besides, twinning matrix experiences severer deformation

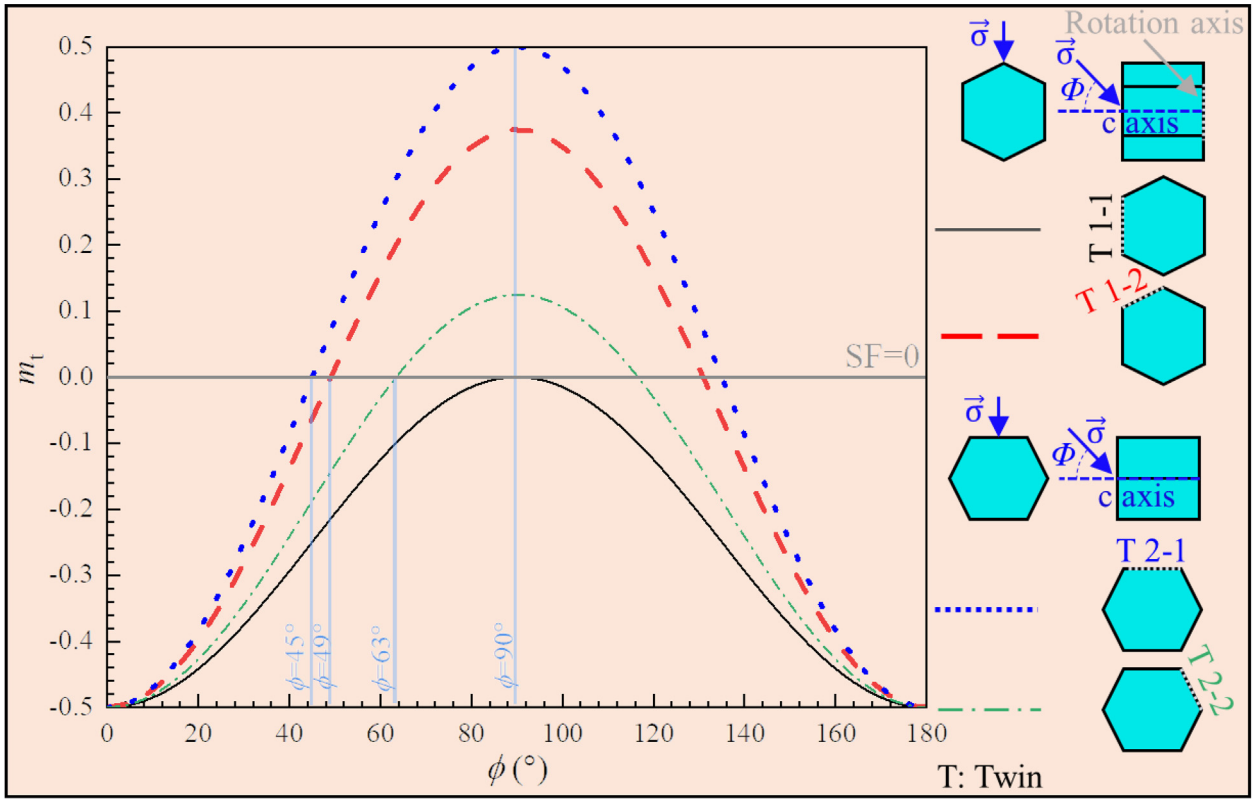


Fig. 10. Twinning Schmid factor (SF) evolutions as tilting angle (Φ) increases from 0° to 180° for four typical twinning types.

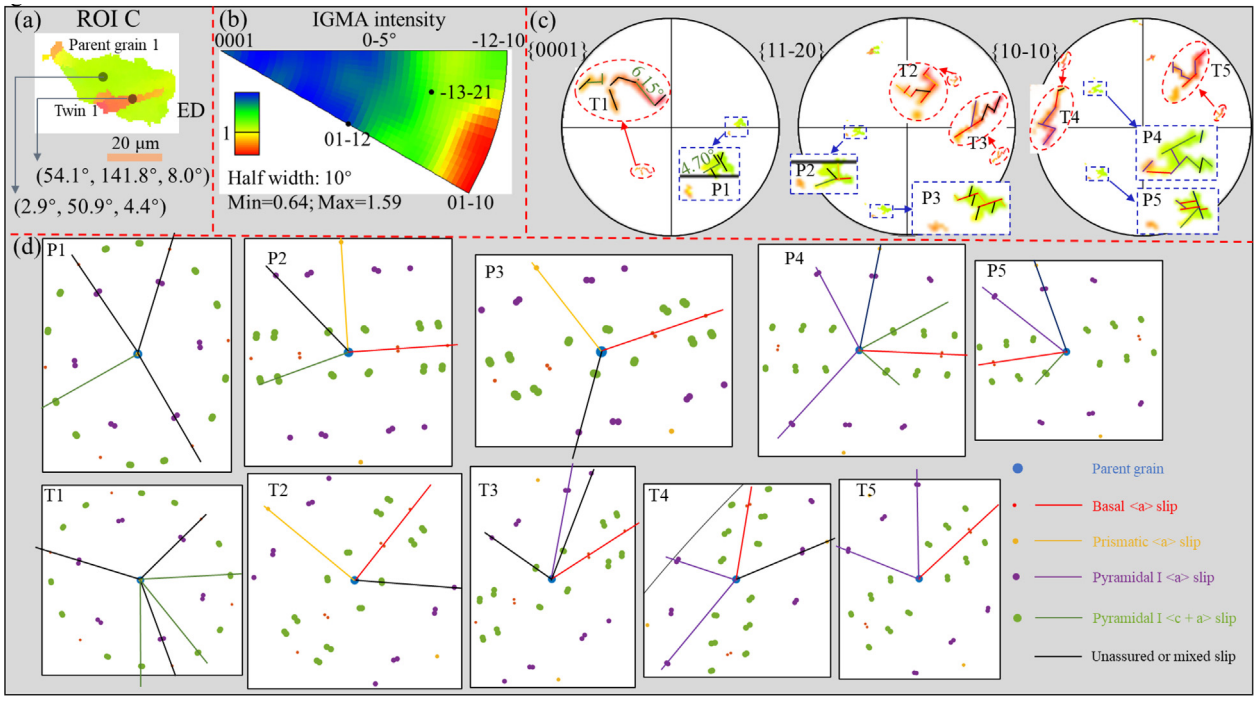


Fig. 11. (a) The IPF-ND map, (b) conventional IGMA and (c, d) modified lattice rotation analysis of ROI C (pure Mg after compression of 12% strain). Note that various slip types are plotted via rotating parent grain along different Taylor axes with a rotation angle of 5° using MTEX inhouse codes.

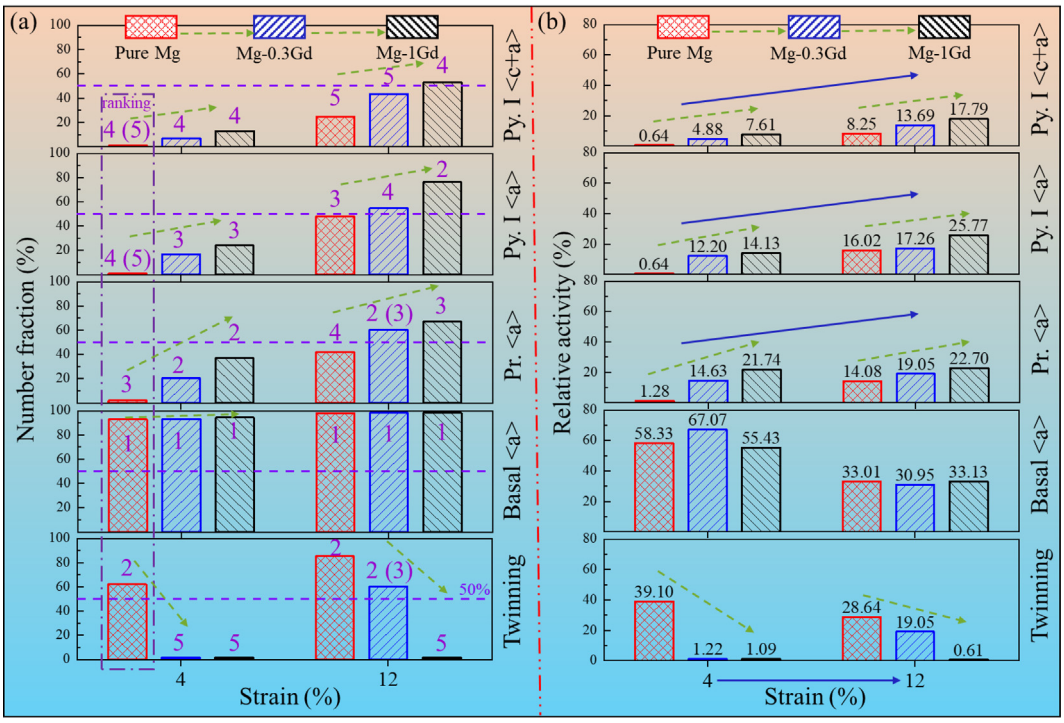


Fig. 12. Summary of the (a) number fractions and (b) relative activities of twinning, basal ⟨a⟩, prismatic ⟨a⟩, pyramidal I ⟨a⟩, and pyramidal I ⟨$c$ + $a$⟩ slips for Mg alloys alloying with various Gd concentrations (0, 0.3, 1, at.%) after compression with 4 and 12% strains, respectively.

compared to grain matrix, as evidenced by higher rotation angle generated by pyramidal I ⟨$c$ + $a$⟩ slip of T1 than that of P1 (Fig. 11), revealing {10–12} twinning behavior accompanies with severer stress concentration.

To further fathom out the quantitative activities of various slip modes, statistical analysis of approx. 500 grains were conducted on the EBSD results of pure Mg, Mg-0.3Gd and Mg-1Gd alloys after compression of 4 and 12% strains (Figs. 6 and 7) using the modified lattice rotation analysis. The obtained number fractions are shown in Fig. 12(a); the relative activity ($F_R^i$, $i$ represents the $i_{th}$ slip (twinning) type) of Fig. 12(b) is determined by normalizing the number fractions ($F_N^i$) of Fig. 12(a) based on following equation:

$$F_R^i = \frac{F_N^i}{\sum_{i=1}^{i_{max}} F_N^i} \tag{6}$$

From Fig. 12(a), with the progress of deformation, the number fractions of both twinning and slip systems increase for all alloys. In addition, with the increase of Gd concentration, under a given compressive strain (i.e., 4%), number fractions of both basal and non-basal slips were increasing, accompanying with evident decreasing twinning number fractions. The former is reasonable considering that higher stress will activate more slip (twinning) systems with low CRSS, based on Schmid law. The latter indicates that as Gd concentration increases, twinning behavior is suppressed while slip behaviors including non-basal slips are activated gradually. Such Gd-activated non-basal slips were mostly ascribed to the decreased anisotropy of basal vs. non-basal dislocation slips [17,18,26]. For example, using the Guiner technique, the addition of Gd was reported to decrease c/a ratio of lattice greatly, thus leading to the decrease regarding the CRSS difference among various slip systems and in turn promoting the activation of non-basal slips [62]. The reduced anisotropy of basal vs. non-basal slips should be fundamentally owing to the electric interactions in $d$-orbits of RE elements with $p$-orbits of Mg and lowered stacking faults energies [63].

After normalization, for pure Mg, the twinning relative activity at 4% compressive strain is higher than that at 12% compressive strain, suggesting the significant role of twinning in the initial stage of deformation in pure Mg; on the contrary, for Mg-0.3Gd alloy, twinning behavior mostly contributes to the posterior stage of deformation (strain≥4%), considering the abnormal increase of twinning relative activity as the deformation progresses from 4 to 12% (cf. Fig. 12(b)). It can be further extrapolated from Fig. 9 that for Mg-1Gd alloy, similarly, twinning behavior mainly plays its role on the stage of more posterior compressive deformation (strain≥12%). These disclose an interesting phenomenon that twinning stage during deformation can be gradually postponed by the increase of Gd concentration, which should be related with Schmid factors (SFs) and CRSS of various deformation systems.

With only the highest SFs of slip systems in each grain being considered for various slip modes, the average macroscopic SFs for Mg-xGd alloys can be determined (Table 4); meanwhile, the highest SFs for tension twinning after considering its polar nature are also tabulated in Table 4. The twinning SF is obviously decreased by the addition of Gd whilst the addition of Gd seems to influence little on the slip SFs. Furthermore, it is generally accepted that the CRSS of various deformation modes follows an increasing trend: basal

Table 4
Summary of the average SFs of various deformation systems for pure Mg, Mg-0.3Gd and Mg-1Gd alloys. Note that only the highest SFs of various slip systems for each grain were collected.

| SFs | Slip types | | | | Tension twinning |
|---|---|---|---|---|---|
| | Basal <a> | Prismatic <a> | Pyramidal I ⟨a⟩ | Pyramidal I ⟨c + a⟩ | |
| Pure Mg | 0.31 | 0.32 | 0.38 | 0.40 | 0.43 |
| Mg-0.3Gd | 0.34 | 0.27 | 0.38 | 0.40 | 0.26 |
| Mg-1Gd | 0.35 | 0.31 | 0.41 | 0.39 | 0.27 |

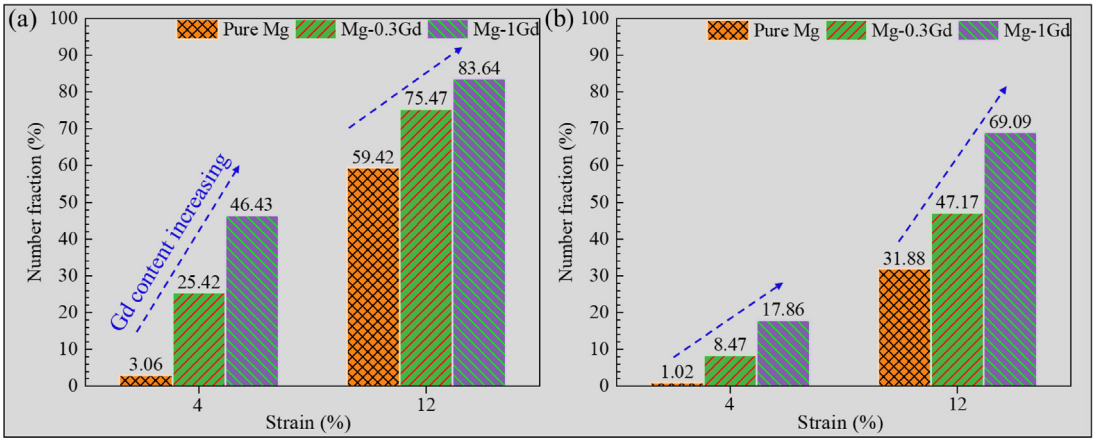


Fig. 13. The number fractions of grain containing (a) two or more and (b) three or more different slip types for pure Mg, Mg-0.3Gd and Mg-1Gd alloys as a function of compressive strain.

⟨a⟩ slip, {10–12} tension twinning, non-basal ⟨a⟩ slip, non-basal ⟨c + a⟩ slip [64,65]. However, this is obviously contradictory to the deferred twinning behavior during deformation of Mg-0.3Gd and Mg-1Gd alloys of this work (Fig. 12(b)), indicating different responses regarding the CRSS of {10–12} tension twin and slip behaviors by the addition of Gd. Similar Gd-delayed onset of twinning phenomenon has been reported by Basu and Al-Samman [66], who ascribed that to the atomic size difference between Mg (approx. 0.16 nm) and Gd (approx. 0.18 nm) as well as the appearance of Gd solute clusters. Furthermore, the impact of RE solute on the intrinsic and extrinsic stacking fault energies as well as the interaction between twinning/slip dislocations and Gd atom were also proposed to make contributions to the transition of deformation behavior [66].

To uncover the influences of applied strain and Gd concentration on the cross-slip activities, Fig. 13 is drawn regarding the number fractions of grain containing (a) two or more and (b) three or more different slip types. Clearly, the number fraction of cross-slip behavior exhibits positive correlations with both compressive strain and alloying Gd concentration. Wu et al. demonstrated that the addition of Gd can effectively decrease the energy barrier between various slip systems and thus enhance cross-slip behavior [8], which is consistent with this study (Fig. 13).

To unmask the relationship between underlying deformation mechanism and GRC, special focus was further placed on the neighboring stress distribution of GRC (Fig. 14). Surprisingly, no obvious stress concentration near GRC is observed, demonstrating GRC plays an poor role on hindering the slip dislocation movements and contributing to hardening behavior, probably owing to their coarse size of GRC along ED (cf. Fig. 4) [67]. On the contrary, obvious stress concentrations can be distinguished along grain boundaries (GBs) in Fig. 14. In previous study, the "local effects" especially grain to grain compatibility are supposed to make considerable contributions for the deformation of Gd-containing Mg alloys [17].

In light of above information, grain 2 of ROI F (Mg-1Gd alloy) was subsequently selected to further analyze the relevance of GB on slip behaviors, as shown in Fig. 15. Fig. 15(b) displays the conventional IGMA distribution of ROI F with the concentration of rotation axis nearing the [0001] and [−13–21] axes, implying amounts of prismatic ⟨a⟩ and pyramidal I ⟨c + a⟩ slips were activated. By using modified lattice rotation analysis, basal ⟨a⟩, prismatic ⟨a⟩, pyramidal I ⟨a⟩ and pyramidal I ⟨c + a⟩ slips are distinguished clearly for parent grain 2 (Fig. 15(e) P7-P9). SFs for all potential slip systems were tabulated in Table 5. Amounts of slips including non-basal slip activities are found to enrich near GBs by comparing the color gradient extended by slip behaviors in pole figures and corresponding IPF map (Fig. 15); besides, the activated slip variants exhibit both low $m$ and low $m$ rankings, especially for pyramidal I ⟨a⟩ and pyramidal I ⟨c + a⟩ slips (Table 5). These indicate non-basal slip activities near ROI F show a close correlation with grain boundaries dominated localized strain/stress. This agrees well with previous study by Koike et al. that substantial cross-slip behaviors in-

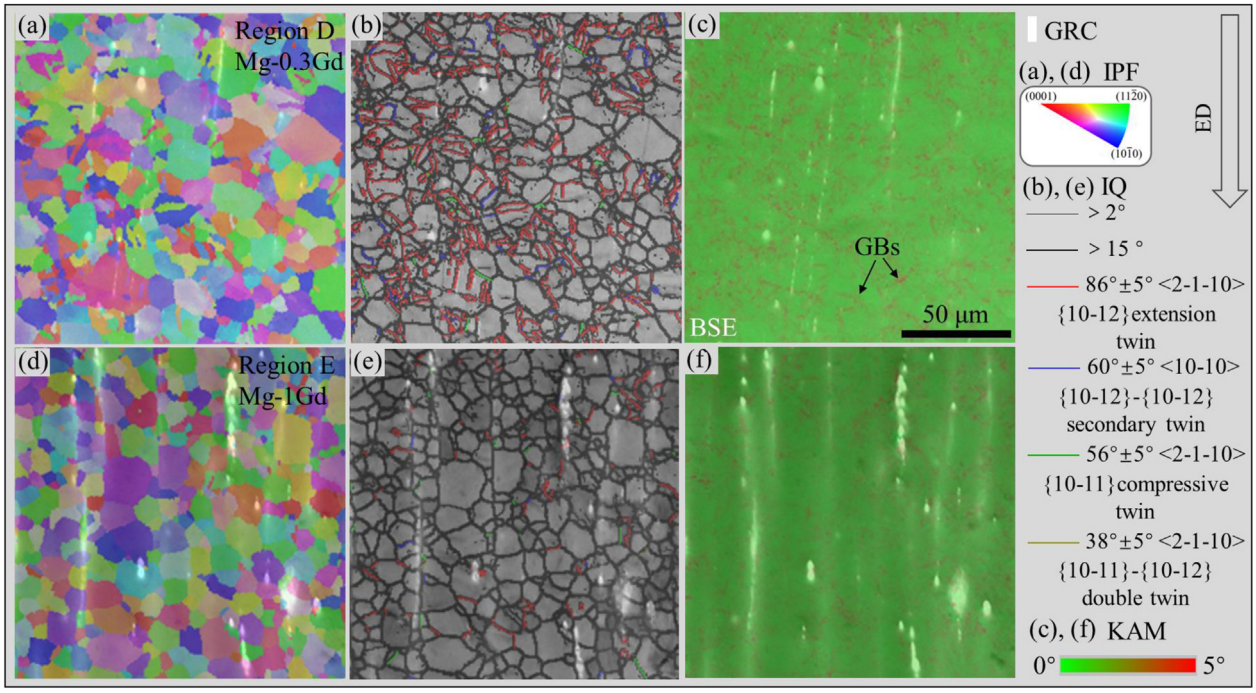


Fig. 14. (a, d) IPF-ND, (b, e) IQ, (c, f) kernel average mis-orientation (KAM) maps shaded with corresponding SEM morphologies under BSE mode of ROI (a-c) D and (d-f) E.

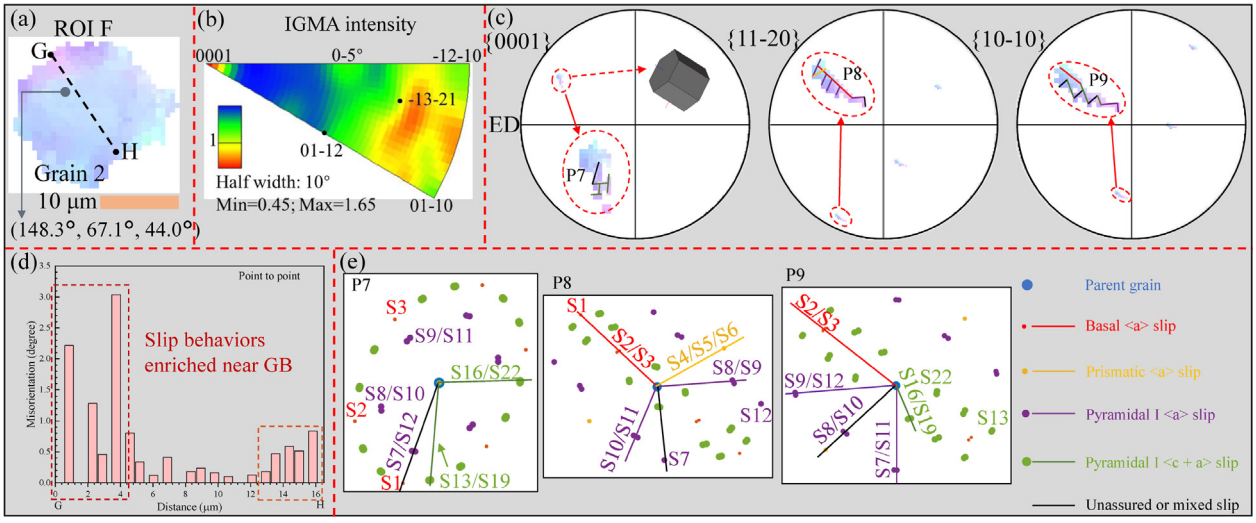


Fig. 15. (a) The IPF-ND map, (b) conventional IGMA and (c, e) modified lattice rotation analysis of ROI F (Mg-1Gd alloy after compression of 12% strain). The misorientation angle distribution along line GH shown in Fig. 15(a) is inserted as Fig. 15(d).

duced by plastic compatibility stress are associated with grain boundaries [34]. The SFs of six theoretical {10–12} twinning variants for grain 2 were presented in Table 6, yet no twin was observed albeit comparable SF values can be found for both twinning and slip systems (Tables 5 and 6). This further indicates the increased CRSS of twin and testifies deferred twinning behavior by the addition of Gd (Fig. 12).

To further reveal the relationship between potential Gd segregation behavior at GB and deformation mechanisms, TEM characterizations on GBs of Mg-0.3Gd and Mg-1Gd alloys were performed (Fig. 16). Clearly, nano GRC displaying like "black beans" along GB can be observed (Fig. 16(d)). Such Gd enrichment behavior near GB was also up-hold by TEM-EDS results (Table 7), which is in line with many previous studies [17,68–72]. It's postulated that nano GRC along GBs exerts a non-negligible role on the deformation behavior [73].

It is generally accepted that the nucleation of both twin and non-basal slips has a strong correlation with GBs. For instance, despite various {10–12} tension twinning nucleation mechanisms being proposed in various studies, a common local stress/strain dominated factor, geometric compatibility factor (m') related with grain boundary, are adopted

Table 5
Calculated SFs of the 24 slip systems in ROI F (Mg-1Gd alloy after compression of 12% strain). SFs of the activated slip system(s) are bolded.

| Slip types | Nominations | Slip plane - slip direction | Taylor axis | Schmid factors of ROI F | Ranking of SF |
|---|---|---|---|---|---|
| Basal | **S1** | **(0001) [2–1–10]** | **[01–10]** | **0.34** | **2** |
| ⟨a⟩ | **S2** | **(0001) [−12–10]** | **[10–10]** | **0.47** | **1** |
| slip | **S3** | **(0001) [−1–120]** | **[1–100]** | **0.14** | **3** |
| Pr. | **S4** | **(01–10) [2–1–10]** | **[0001]** | **0.19** | **1** |
| ⟨a⟩ | **S5** | **(10–10) [−12–10]** | **[0001]** | **0.09** | **3** |
| slip | **S6** | **(1–100) [−1–120]** | **[0001]** | **0.10** | **2** |
| Py. | **S7** | **(01–11) [2–1–10]** | **[0–112]** | **0.01** | **6** |
| I | **S8** | **(−1011) [−12–10]** | **[10–12]** | **0.14** | **4** |
| ⟨a⟩ | **S9** | **(1–101) [−1–120]** | **[−1102]** | **0.17** | **3** |
| slip | **S10** | **(10–11) [−12–10]** | **[−1012]** | **0.30** | **2** |
| | **S11** | **(−1101) [−1–120]** | **[1–102]** | **0.03** | **5** |
| | S12 | (0–111) [2–1–10] | [01–12] | 0.33 | 1 |
| Py. | **S13** | **(10–1–1) [−211–3]** | **[1–32–1]** | **0.21** | **7** |
| I | S14 | (1–101) [−2113] | [12–31] | 0.40 | 2 |
| $\langle c+a \rangle$ | S15 | (0–111) [11–23] | [3–2–1–1] | 0.44 | 1 |
| slip | **S16** | **(0–111) [1–21–3]** | **[3–1–21]** | **0.27** | **5** |
| | S17 | (1–101) [1–21–3] | [21–3–1] | 0.34 | 4 |
| | S18 | (10–1–1) [11–23] | [2–311] | 0.14 | 9(10) |
| | **S19** | **(10–11) [−2113]** | **[−13–2–1]** | **0.22** | **6** |
| | S20 | (1–10–1) [−211–3] | [−1–231] | 0.14 | 9(10) |
| | S21 | (01–11) [11–2–3] | [−321–1] | 0.02 | 12 |
| | **S22** | **(01–11) [1–213]** | **[−3121]** | **0.03** | **11** |
| | S23 | (1–10–1) [1–213] | [−2–13–1] | 0.15 | 8 |
| | S24 | (10–11) [11–2–3] | [−23–11] | 0.39 | 3 |

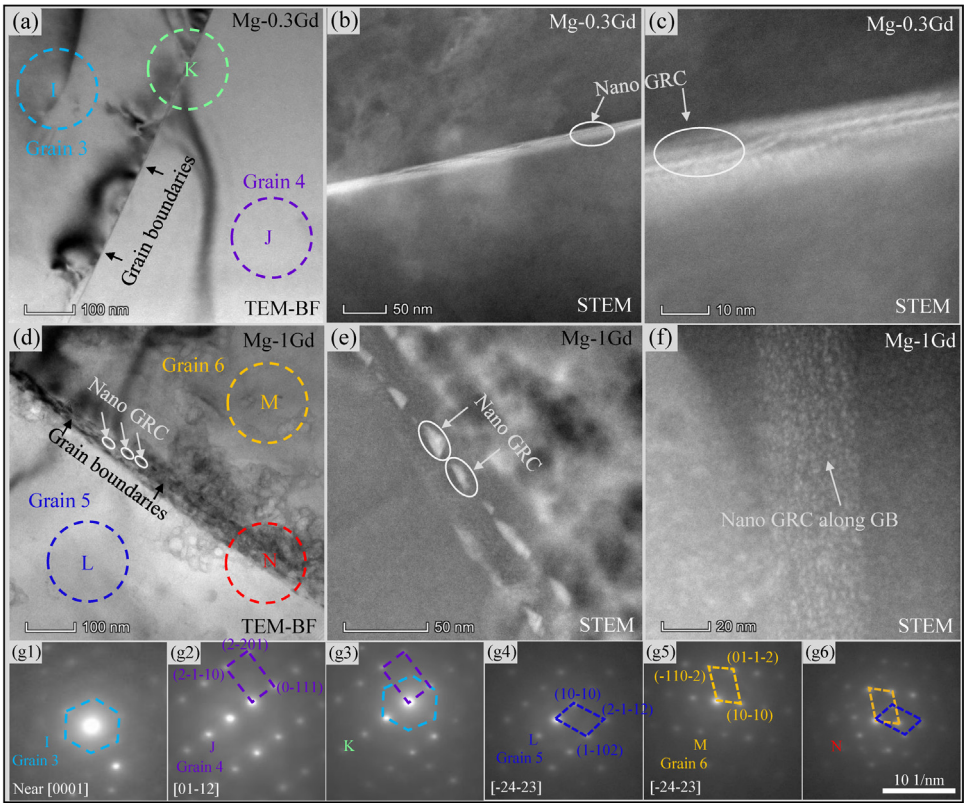


Fig. 16. (a, d) TEM and (b, c, e, f) scanning transmission electron microscopy (STEM) micrographs of nano GRC near grain boundaries for (a-c) Mg-0.3Gd and (d-f) Mg-1Gd alloys. (g1-g6) Selected area electron diffraction (SAED) patterns of ROI (g1) I, (g2) J, (g3) K (g4) L, (g5) M and (g6) N.

Table 6
The SFs of six theoretical {10–12} twinning variants regarding grain 2.

| Twinning systems | Twinning plane - twinning direction | (−1012) [10–11] | (10–12) [−1011] | (1–102) [−1101] | (−1102) [1–101] | (01–12) [0–111] | (0–112) [01–11] |
|---|---|---|---|---|---|---|---|
| | Rotation axes | [−12–10] | [1–210] | [−1–120] | [11–20] | [2–1–10] | [−2110] |
| SFs | | 0.30 | 0.29 | 0.10 | 0.16 | 0.23 | 0.18 |

Table 7
Gd concentrations of studied alloys for the matrix and grain boundary measured using TEM-EDS. The value before and after plus-minus sign represents the average and standard deviations of TEM-EDS results.

| Alloys | Matrix (at.%) | Grain boundary (at.%) |
|---|---|---|
| Pure Mg | – | – |
| Mg-0.3Gd | 0.22 ± 0.02 | 0.28 ± 0.05 |
| Mg-1Gd | 0.98 ± 0.03 | 1.53 ± 0.14 |

Table 8
Summary of the contributions of various strengthening factors on yield strengths of pure Mg, Mg-0.3Gd and Mg-1Gd alloys in this work.

| Alloys | $d$ ($\mu$m) | $\sigma_y$ (MPa) | $\sigma_0$ (MPa) | $\Delta\sigma_{gb}$ (MPa) | $\Delta\sigma_{ss}$ (MPa) | $\Delta\sigma_{de}$ (MPa) |
|---|---|---|---|---|---|---|
| Pure Mg | 27.64 | 36.00 | 8.00 | 30.05 | 0 | −2.05 |
| Mg-0.3Gd | 6.50 | 94.00 | | 61.97 | 19.76 | 4.27 |
| Mg-1Gd | 8.43 | 121.00 | | 54.42 | 53.49 | 5.09 |

to explain twinning nucleation behavior [73–75]; and grain boundaries are also reported to be preferred sites for the onset of slip dislocations nucleation [76]. Besides, by using ab initio software, the {10–12} ⟨10–11⟩ tension twin of Mg was determined as atomic shuffling-controlled [77]. Consequently, the atomic shuffling characteristic of {10–12} tension twins decides the critical importance of atomic constitution near twinning embryo, that is, grain boundaries [78]. Combining the delayed onset of twinning behavior by Gd (cf. Fig. 12), it's postulated that nano GRC along grain boundaries may cause higher activation energies and CRSS for twinning nucleation, owing to the elastic and electric interactions [76]. Unlike {10–12} tension twins, the slip dislocations are commonly associated with simply shearing mechanism. Previous study regarding Mg-RE alloy have reported the addition of RE can reduce the CRSS of non-basal slip systems [79]. This fundamental inconsistency regarding nucleation and propagation mechanisms should have induced opposite impacts on the CRSS of {10–12} tension twin and slip behaviors, despite similar Gd segregation condition at GB, leading to the gradually deferred twinning behavior as Gd content increases. Besides, the dominant twinning mode was recently reported to switch from {10–12} twinning to {11–21} twinning, with the Gd concentration increasing from 0 to 14 wt.% in Mg alloy [80]. The transformation of twinning mode is probably related with the delayed twinning behavior in this work, although no {11–21} twinning mode is observed for all alloys after compression with 12% strain (Fig. 7).

Except the above-mentioned factors affecting slip (twinning) behavior, the grain size, texture, second phase and solute Gd of alloy, etc. may also have effects on the deformation behavior and mechanical properties of alloy [17,81–85]. For example, with decreasing the grain size from 19 to 5 $\mu$m, a transition from twinning to basal slip, localized along deformation bands, was found to take place for pure Mg [81]. The influences of these factors on deformation behavior and mechanical properties will be discussed thoroughly combined with increasing Gd concentration, as schematically illustrated in Fig. 17. In terms of initial state, the alloying of Gd weakens the basal texture, refines grain size, and introduces GRC especially in nano-size along GBs. With Gd content increases, twinning-prevailing stage is postponed to higher strain and concomitantly the activities of non-basal slips are significantly enhanced especially during early stage of deformation, as quantitatively determined using modified lattice rotation analysis (cf. Fig. 12). Additionally, both the strength and ductility are positively correlated with the concentration of Gd, whose origins will be discussed in what follows.

In the regard of improved yield strength ($\sigma_y$) by alloying Gd, several factors should be taken into considerations as following equation:

$$\sigma_y = \sigma_0 + \Delta\sigma_{gb} + \Delta\sigma_{ss} + \Delta\sigma_{de} \quad (7)$$

where $\sigma_0$ is the friction stress representing the resistance of the lattice to dislocation movement (8 MPa[25]), $\Delta\sigma_{gb}$ and $\Delta\sigma_{ss}$ represent the stress contributions by grain size reduction and Gd solid solution strengthening, respectively, $\Delta\sigma_{de}$ is the deviation between experimental yield stress ($\sigma_y$) and the sum of $\sigma_0$, $\Delta\sigma_{gb}$ and $\Delta\sigma_{ss}$ to verify the reliability of calculation. According to Hall-Petch formula, the influence of grain size on $\Delta\sigma_{gb}$ can be described by the following equation:

$$\Delta\sigma_{gb} = k \cdot d^{-1/2} \quad (8)$$

where $k$ is the material constant (0.188 MPa•m$^{1/2}$[25]) and $d$ is the average grain diameter of alloy. Besides, the increase of yield strength by Gd solid solution strengthening ($\Delta\sigma_{ss}$) can be calculated from Labusch's approach[86]:

$$\Delta\sigma_{ss} = B_{Gd} \cdot x_{Gd}^{2/3} \quad (9)$$

where $B_{Gd}$ is a constant for element Gd (1168 MPa•at.$^{-2/3}$ [87]) and $x_{Gd}$ is the atomic fraction of solute Gd (0.22 and 0.98 at.% for Mg-0.3Gd and Mg-1Gd alloys' matrix, respectively, cf. Table 7). As tabulated in Table 8, the combination of grain boundary hardening ($\Delta\sigma_{gb}$) and solid solution strengthening ($\Delta\sigma_{ss}$) accounts for most of yield strength for pure Mg,

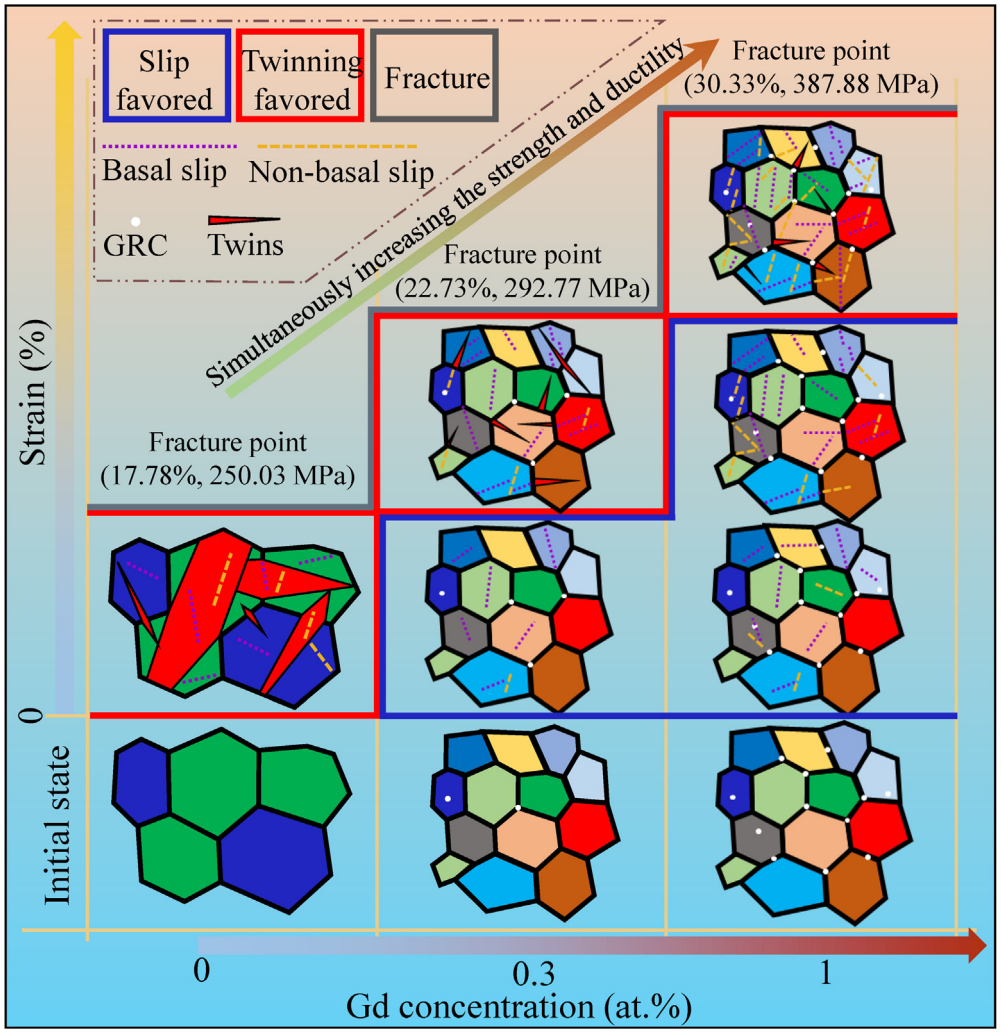


Fig. 17. Schematic diagram illustrating the evolution of deformation mechanisms with the increasing of Gd concentration and applied strain.

Mg-0.3Gd and Mg-1Gd alloys. The negative value of $\Delta\sigma_{de}$ for pure Mg should be resulting from the broad distribution of grain size (cf. Fig. 2(d)) whilst the slight high positive values of $\Delta\sigma_{de}$ for Mg-0.3Gd and Mg-1Gd alloys are owing to the dispersion strengthening by Gd-rich nano clusters along GBs (cf. Fig. 16).

Regarding the increasing ductility with Gd concentration increasing, following four possible factors will be discussed in details:

The weakened basal texture by Gd addition can influence the deformation behavior by changing the macroscopic SFs of slip (twinning) systems (cf. Table 4). The twinning SFs is observed to be obviously decreased by alloying Gd, indicating higher stress will be needed to activate the twinning behavior under the premise of same twinning CRSS for Mg-xGd alloys. This can partly explain the delayed twinning behavior after alloying Gd. However, such role on slip activities is limited considering comparable SFs of slips for Mg-xGd alloys (Table 4). Note that the explanation of simply weakened basal texture cannot uphold the further postponed twinning-prevailing stage and improved ductility as Gd concentration increases from 0.3 to 1 at.%, whose alloys share similar recrystallization texture thus comparable slip (twinning) SFs yet display different deformation behaviors and fracture strains. Despite that, the weakened basal texture by alloying Gd still exerts its role for improved ductility to some extent.

The reduction of grain size by alloying Gd should have also contributed to the improved ductility. Recent study revealed that the total elongation of pure Mg increases almost linearly with the negative square root of grain size ($d^{-1/2}$; $d \geq 4.32$ $\mu$m) [88]; a nearly twofold increase in ductility can be expected for pure Mg when the average grain size refines from 27.64 to 6.50 $\mu$m, accompanying with the weakened twinning activities and enhanced activities of both non-basal slips and grain boundary sliding (GBS) behaviors [34,88,89]. This could explain higher fracture strains of Gd-bearing Mg alloys compared with pure Mg to some extent. However, in comparison to Mg-0.3Gd alloy, the bigger grain size and similar recrystallization texture of Mg-1Gd alloys reveals other factors should be considered for the highest ductility of Mg-1Gd alloy.

Except the abovementioned role of activating non-basal slips by reducing grain size, the addition of Gd is postulated to intrinsically reduce the anisotropy of basal vs. non-basal dislocation slips, as reported in many previous studies [17,18,26,62]. The addition of Gd was also determined to decrease cross-slip barrier ($\Delta G_{xs}$) and promote different sliding pathways in the Mg-Gd alloy [8]. Similarly, the obviously increased number fractions of double-slips and triple-slips by the addition of Gd (Fig. 13) should be correlated with the reduced anisotropy of basal vs. non-basal dislocation slips thus improved ductility.

The deferred twinning behavior by the alloying of Gd is regarded as another significant factor for the improvement of ductility. In comparison with slip behavior, twinning behavior is generally known as more heterogenous deformation modes with severer stress concentration, as evidenced by Fig. 11. Recent study has also shown that the weakened twinning behavior and enhanced non-basal slips activities can effectively aid in homogenization of stress distribution and the enhancement of ductility [90]. Therefore, the deferred and weakened twinning behavior accompanying with posterior and weakened stress concentration should be another important factor accounting for the high ductility. It is worthy mentioned that the weakened twinning behavior should be a combined effect of multi factors (i.e. reduced twinning SFs, refined grain size, intrinsically altered anisotropy of basal vs. non-basal dislocation slips, grain boundary segregation of Gd, etc.), which should be fundamentally ascribed to the alloying of Gd. And their individual weighting factors on weakening and postponing twinning behavior desire further investigations.

## 4. Conclusion

We reported a modified lattice rotation analysis that can distinguish all slip systems and provide statistical results for slip and twinning activities in Mg-xGd alloys. Using this method, the underlying deformation mechanisms associated with the enhanced ductility of Mg alloy by Gd addition is quantitatively clarified, and the main conclusions are reached as follows:

(1) Twinning behavior was quantitatively determined to be postponed in Mg-Gd alloy by Gd addition, leading to posterior and weakened stress concentration thus high ductility.

(2) Obvious cross-slip behaviors were determined in Mg-Gd alloy, related with the intrinsically decreased anisotropy of basal vs. non-basal dislocation slips by Gd addition.

(3) The transition of deformation behavior by alloying Gd should be linked with multi factors, which can be fundamentally ascribed to the addition of Gd.

(4) Gd-driven high strength could be primarily ascribed to the grain size refinement and solute solution strengthening. The reduced grain size, weakened basal texture, intrinsically decreased anisotropy of basal vs. non-basal slips and delay of twinning behavior should be mainly responsible for high ductility of Mg-Gd alloy.

## Acknowledgements

This investigation is supported by the grant from the Natural Science Foundation of China (51871244), the Hunan Provincial Innovation Foundation for Postgraduate (CX20200172), and the Fundamental Research Funds for the Central Universities of Central South University (1053320190103).

## References

[1] J. Song, J. She, D. Chen, F. Pan, J Magnes Alloys. 8 (2020) 1–41, doi:10.1016/j.jma.2020.02.003.
[2] T. Xu, Y. Yang, X. Peng, J. Song, F. Pan, J Magnes Alloys. 7 (2019) 536–544, doi:10.1016/j.jma.2019.08.001.
[3] G. Wu, C. Wang, M. Sun, W. Ding, J Magnes Alloys. 9 (2021) 1–20, doi:10.1016/j.jma.2020.06.021.
[4] Z. Wu, W.A. Curtin, Nature 526 (2015) 62–67, doi:10.1038/nature15364.
[5] R.V. Mises, ZAMM - J Appl Math Mech Z Für Angew Math Mech 8 (1928) 161–185, doi:10.1002/zamm.19280080302.
[6] G.W. Groves, A. Kelly, Philos Mag J Theor Exp Appl Phys 8 (1963) 877–887, doi:10.1080/14786436308213843.
[7] R. Ahmad, B. Yin, Z. Wu, W.A. Curtin, Acta Mater 172 (2019) 161–184, doi:10.1016/j.actamat.2019.04.019.
[8] Z. Wu, R. Ahmad, B. Yin, S. Sandlöbes, W.A. Curtin, Science 359 (2018) 447–452, doi:10.1126/science.aap8716.
[9] N. Zhou, Z. Zhang, L. Jin, J. Dong, B. Chen, W. Ding, Mater Des 56 (2014) 966–974 1980-2015, doi:10.1016/j.matdes.2013.12.014.
[10] G. Zhu, L. Wang, H. Zhou, J. Wang, Y. Shen, P. Tu, H. Zhu, W. Liu, P. Jin, X. Zeng, Int J Plast 120 (2019) 164–179, doi:10.1016/j.ijplas.2019.04.020.
[11] Z.R. Zeng, M.Z. Bian, S.W. Xu, C.H.J. Davies, N. Birbilis, J.F. Nie, Mater Sci Eng A 674 (2016) 459–471, doi:10.1016/j.msea.2016.07.049.
[12] Q. Wang, Y. Mu, J. Lin, L. Zhang, H.J. Roven, Mater Sci Eng A 699 (2017) 26–30, doi:10.1016/j.msea.2017.05.080.
[13] S. Sandlöbes, M. Friák, S. Korte-Kerzel, Z. Pei, J. Neugebauer, D. Raabe, Sci Rep 7 (2017), doi:10.1038/s41598-017-10384-0.
[14] Z. Ding, W. Liu, H. Sun, S. Li, D. Zhang, Y. Zhao, E.J. Lavernia, Y. Zhu, Acta Mater 146 (2018) 265–272, doi:10.1016/j.actamat.2017.12.049.
[15] H.S. Jang, B.J. Lee, Scr Mater 160 (2019) 39–43, doi:10.1016/j.scriptamat.2018.09.022.
[16] H.S. Jang, J.K. Lee, A.J.S.F. Tapia, N.J. Kim, B.-J. Lee, J Magnes Alloys. (2021), doi:10.1016/j.jma.2021.03.007.
[17] N. Stanford, D. Atwell, M.R. Barnett, Acta Mater 58 (2010) 6773–6783, doi:10.1016/j.actamat.2010.09.003.
[18] K. Luo, L. Zhang, G. Wu, W. Liu, W. Ding, J Magnes Alloys. 7 (2019) 345–354, doi:10.1016/j.jma.2019.03.002.
[19] H. Yu, Y. Hongge, C. Jihua, S. Bin, Z. Yi, S. Yanjin, M. Zhaojie, J Alloys Compd 586 (2014) 757–765, doi:10.1016/j.jallcom.2013.10.005.
[20] C. Junxiu, T. Lili, Y. Xiaoming, Y. Ke, J Mater Sci Technol 35 (2019) 503–511, doi:10.1016/j.jmst.2018.10.022.
[21] L.K. Singh, A. Bhadauria, A. Srinivasan, U.T.S. Pillai, B.C. Pai, Int J Miner Metall Mater 24 (2017) 901–908, doi:10.1007/s12613-017-1476-4.
[22] H. Yan, R. Chen, N. Zheng, J. Luo, S. Kamado, E. Han, J Magnes Alloys 1 (2013) 23–30, doi:10.1016/j.jma.2013.02.003.
[23] H.S. Jiang, X.G. Qiao, M.Y. Zheng, K. Wu, C. Xu, S. Kamado, Mater Charact 135 (2018) 96–103, doi:10.1016/j.matchar.2017.11.025.
[24] R.H. Buzolin, M. Mohedano, C.L. Mendis, B. Mingo, D. Tolnai, C. Blawert, K.U. Kainer, H. Pinto, N. Hort, Mater Sci Eng A 682 (2017) 238–247, doi:10.1016/j.msea.2016.11.022.
[25] A. Kula, K. Noble, R.K. Mishra, M. Niewczas, Philos Mag 96 (2016) 134–165, doi:10.1080/14786435.2015.1123820.

[26] L. Tang, W. Liu, Z. Ding, D. Zhang, Y. Zhao, E.J. Lavernia, Y. Zhu, Comput Mater Sci 115 (2016) 85–91, doi:10.1016/j.commatsci.2016.01.003.
[27] A. Akhtar, E. Teghtsoonian, Acta Metall 17 (1969) 1351–1356, doi:10.1016/0001-6160(69)90152-7.
[28] A. Akhtar, E. Teghtsoonian, Acta Metall 17 (1969) 1339–1349, doi:10.1016/0001-6160(69)90151-5.
[29] A. Akhtar, E. Teghtsoonian, Philos Mag J Theor Exp Appl Phys 25 (1972) 897–916, doi:10.1080/14786437208229311.
[30] Y. Wu, W. Hu, Eur Phys J B 57 (2007) 305–312, doi:10.1140/epjb/e2007-00164-9.
[31] S.W. Lee, S.-.H. Kim, W.-.K. Jo, W.-.H. Hong, W. Kim, B.G. Moon, S.H. Park, J Alloys Compd 791 (2019) 700–710, doi:10.1016/j.jallcom.2019.03.316.
[32] S. Jiang, Y. Jia, X. Wang, J. Jiang, Mater. Charact. 165 (2020) 110384, doi:10.1016/j.matchar.2020.110384.
[33] H. Wang, C.J. Boehlert, Q.D. Wang, D.D. Yin, W.J. Ding, Mater Charact 116 (2016) 8–17, doi:10.1016/j.matchar.2016.04.001.
[34] J. Koike, T. Kobayashi, T. Mukai, H. Watanabe, M. Suzuki, K. Maruyama, K. Higashi, Acta Mater 51 (2003) 2055–2065, doi:10.1016/S1359-6454(03)00005-3.
[35] K.X. Sun, Y. Zeng, D.D. Yin, F. Gao, L.J. Long, X.Y. Qian, Y.J. Wan, G.F. Quan, B. Jiang, Mater Sci Eng A 792 (2020) 139801, doi:10.1016/j.msea.2020.139801.
[36] J.H. Hwang, A. Zargaran, G. Park, O. Lee, B.-J. Lee, N.J. Kim, J Magnes Alloys. (2020), doi:10.1016/j.jma.2020.09.016.
[37] S. Jiang, Y. Jia, X. Wang, J Magnes Alloys. 8 (2020) 1186–1197, doi:10.1016/j.jma.2020.01.002.
[38] Y.B. Chun, M. Battaini, C.H.J. Davies, S.K. Hwang, Metall Mater Trans A 41 (2010) 3473–3487, doi:10.1007/s11661-010-0410-4.
[39] Y.B. Chun, C.H.J. Davies, Springer International Publishing, Cham, 2016, pp. 345–349, doi:10.1007/978-3-319-48099-2_55.
[40] M. Zhang, B. Luan, L. Chu, B. Gao, L. Wang, G. Yuan, Q. Liu, Scr Mater 187 (2020) 379–383, doi:10.1016/j.scriptamat.2020.06.050.
[41] E.J. Rapperport, C.S. Hartley, Trans Met Soc AIME 218 (1960) 869–877 Vol: https://www.osti.gov/biblio/4156895-deformation-modes-zirconium . (accessed January 26, 2021).
[42] U.M. Chaudry, Y.S. Kim, K. Hamad, Mater Lett 238 (2019) 305–308, doi:10.1016/j.matlet.2018.12.013.
[43] X. Zeng, P. Minárik, P. Dobroň, D. Letzig, K.U. Kainer, S. Yi, Scr Mater 166 (2019) 53–57, doi:10.1016/j.scriptamat.2019.02.045.
[44] D. Guan, W.M. Rainforth, L. Ma, B. Wynne, J. Gao, Acta Mater 126 (2017) 132–144, doi:10.1016/j.actamat.2016.12.058.
[45] C. Zhao, Z. Li, J. Shi, X. Chen, T. Tu, Z. Luo, R. Cheng, A. Atrens, F. Pan, J Magnes Alloys. 7 (2019) 672–680, doi:10.1016/j.jma.2019.09.004.
[46] F. Liu, C. Guo, R. Xin, G. Wu, Q. Liu, J Magnes Alloys. 7 (2019) 258–263, doi:10.1016/j.jma.2019.02.004.
[47] B. Zhou, L. Wang, W. Liu, X. Zeng, Y. Li, Metall Mater Trans A. 51 (2020) 4414–4421, doi:10.1007/s11661-020-05907-w.
[48] F. Bachmann, R. Hielscher, H. Schaeben, Solid State Phenom 160 (2010) 63–68, doi:10.4028/www.scientific.net/SSP.160.63.
[49] G. Proust, Science 365 (2019) 30–31, doi:10.1126/science.aax9732.
[50] M.G. Jiang, C. Xu, H. Yan, T. Nakata, Z.W. Chen, C.S. Lao, R.S. Chen, S. Kamado, E.H. Han, J Magnes Alloys. (2020), doi:10.1016/j.jma.2020.09.001.
[51] Y. Zhang, H. Jiang, Q. Kang, Y. Wang, Y. Yang, S. Tian, J Magnes Alloys. 8 (2020) 769–779, doi:10.1016/j.jma.2019.11.015.
[52] A. Maldar, L. Wang, G. Zhu, X. Zeng, J Magnes Alloys. 8 (2020) 210–218, doi:10.1016/j.jma.2019.07.009.
[53] M.H. Barezban, R. Roumina, H. Mirzadeh, R. Mahmudi, Met Mater Int (2019), doi:10.1007/s12540-019-00479-w.
[54] A. Kula, T. Tokarski, M. Niewczas, Metall Mater Trans A. 51 (2020) 3742–3748, doi:10.1007/s11661-020-05815-z.
[55] J. Min, L.G. Hector, J. Lin, J.T. Carter, A.K. Sachdev, Int J Plast 57 (2014) 52–76, doi:10.1016/j.ijplas.2014.02.004.
[56] D. Drozdenko, P. Dobroň, K. Fekete, S. Yi, J. Bohlen, Twinning–Detwinning in pre-compressed and thermally treated ZX10 and ZN10 Alloys, 13 (2020) 5605. https://doi.org/10.3390/ma13245605.
[57] J.W. Christian, S. Mahajan, Prog Mater Sci 39 (1995) 1–157 https://doi.org/10.1016/0079-6425(94)00007-7.
[58] A. Ghaderi, M.R. Barnett, Acta Mater 59 (2011) 7824–7839, doi:10.1016/j.actamat.2011.09.018.
[59] K.D. Molodov, T. Al-Samman, D.A. Molodov, S. Korte-Kerzel, Acta Mater 134 (2017) 267–273, doi:10.1016/j.actamat.2017.05.041.
[60] Y. Pei, A. Godfrey, J. Jiang, Y.B. Zhang, W. Liu, Q. Liu, Mater Sci Eng A 550 (2012) 138–145, doi:10.1016/j.msea.2012.04.046.
[61] B. Yang, C. Shi, S. Zhang, J. Hu, J. Teng, Y. Cui, Y. Li, A. Chiba, J Magnes Alloys. (2021), doi:10.1016/j.jma.2021.01.006.
[62] F. Hehmann, F. Sommer, B. Predel, Mater Sci Eng A 125 (1990) 249–265, doi:10.1016/0921-5093(90)90175-3.
[63] T. Tsuru, D.C. Chrzan, Sci Rep 5 (2015) 8793, doi:10.1038/srep08793.
[64] M. Arul Kumar, I.J. Beyerlein, R.A. Lebensohn, C.N. Tomé, in: K.N. Solanki, D. Orlov, A. Singh, N.R. Neelameggham (Eds.), Magnes. Technol. 2017, Springer International Publishing, Cham, 2017, pp. 159–165, doi:10.1007/978-3-319-52392-7_25.
[65] M. Arul Kumar, I.J. Beyerlein, R.A. Lebensohn, C.N. Tomé, Mater Sci Eng A. 706 (2017) 295–303, doi:10.1016/j.msea.2017.08.084.
[66] I. Basu, T. Al-Samman, Mater Sci Eng A 707 (2017) 232–244, doi:10.1016/j.msea.2017.09.053.
[67] D. Canadinc, H. Sehitoglu, I. Karaman, Y.I. Chumlyakov, H.J. Maier, Metall Mater Trans A. 34 (2003) 1821–1831, doi:10.1007/s11661-003-0148-3.
[68] M. Bugnet, A. Kula, M. Niewczas, G.A. Botton, Acta Mater 79 (2014) 66–73, doi:10.1016/j.actamat.2014.06.004.
[69] J.P. Hadorn, T.T. Sasaki, T. Nakata, T. Ohkubo, S. Kamado, K. Hono, Scr Mater 93 (2014) 28–31, doi:10.1016/j.scriptamat.2014.08.022.
[70] I. Basu, K.G. Pradeep, C. Mießen, L.A. Barrales-Mora, T. Al-Samman, Acta Mater 116 (2016) 77–94, doi:10.1016/j.actamat.2016.06.024.
[71] J.D. Robson, S.J. Haigh, B. Davis, D. Griffiths, Metall Mater Trans A. 47 (2016) 522–530, doi:10.1007/s11661-015-3199-3.
[72] J.F. Nie, Y.M. Zhu, J.Z. Liu, X.Y. Fang, Science 340 (2013) 6, doi:10.1126/science.1229369.
[73] J. Luster, M.A. Morris, Metall Mater Trans A 26 (1995) 1745–1756, doi:10.1007/BF02670762.
[74] D. Guan, B. Wynne, J. Gao, Y. Huang, W.M. Rainforth, Acta Mater 170 (2019) 1–14, doi:10.1016/j.actamat.2019.03.018.
[75] M. Arul Kumar, M. Gong, I.J. Beyerlein, J. Wang, C.N. Tomé, Acta Mater 168 (2019) 353–361, doi:10.1016/j.actamat.2019.02.037.
[76] H. Somekawa, D.A. Basha, A. Singh, T. Tsuru, M. Yamaguchi, Mater Trans 61 (2020) 1172–1175, doi:10.2320/matertrans.MT-M2020040.
[77] A. Ishii, J. Li, S. Ogata, Int J Plast 82 (2016) 32–43, doi:10.1016/j.ijplas.2016.01.019.
[78] Y. He, B. Li, C. Wang, S.X. Mao, Nat Commun 11 (2020) 2483, doi:10.1038/s41467-020-16351-0.
[79] R.K. Sabat, A.P. Brahme, R.K. Mishra, K. Inal, S. Suwas, Acta Mater 161 (2018) 246–257, doi:10.1016/j.actamat.2018.09.023.
[80] C. He, Z. Li, D. Kong, X. Zhao, H. Chen, J.-.F. Nie, Scr Mater 191 (2021) 62–66, doi:10.1016/j.scriptamat.2020.08.041.
[81] C.M. Cepeda-Jiménez, J.M. Molina-Aldareguia, M.T. Pérez-Prado, Acta Mater 88 (2015) 232–244, doi:10.1016/j.actamat.2015.01.032.
[82] J.D. Robson, N. Stanford, M.R. Barnett, Acta Mater 59 (2011) 1945–1956, doi:10.1016/j.actamat.2010.11.060.
[83] J.D. Robson, M.R. Barnett, Adv Eng Mater 21 (2019) 1800460, doi:10.1002/adem.201800460.
[84] X. Guo, A. Chapuis, P. Wu, Q. Liu, X. Mao, Mater Des 98 (2016) 333–343, doi:10.1016/j.matdes.2016.03.045.
[85] T.R. Bieler, P. Eisenlohr, C. Zhang, H.J. Phukan, M.A. Crimp, Curr Opin Solid State Mater Sci 18 (2014) 212–226, doi:10.1016/j.cossms.2014.05.003.
[86] R. Labusch, Phys Status Solidi B. 41 (1970) 659–669, doi:10.1002/pssb.19700410221.

[87] I. Toda-Caraballo, E.I. Galindo-Nava, P.E.J. Rivera-Díaz-del-Castillo, Acta Mater 75 (2014) 287–296, doi:10.1016/j.actamat.2014.04.064.
[88] R. Zheng, J.-.P. Du, S. Gao, H. Somekawa, S. Ogata, N. Tsuji, Acta Mater 198 (2020) 35–46, doi:10.1016/j.actamat.2020.07.055.
[89] J. Koike, Metall Mater Trans A 36 (2005) 1689–1696, doi:10.1007/s11661-005-0032-4.
[90] M. Lentz, M. Risse, N. Schaefer, W. Reimers, I.J. Beyerlein, Nat Commun 7 (2016) 11068, doi:10.1038/ncomms11068.